Data and Signal Processing of Rotating Shadowband Spectroradiometer (RSS) Data

Piotr W. Kiedron*, Lee H. Harrison, Joseph J. Michalsky, James A. Schlemmer and Jerry L. Berndt
Atmospheric Sciences Research Center

ABSTRACT

The Rotating Shadowband Spectroradiometer (RSS) is a tandem-prisms spectrograph that uses a CCD array to measure solar direct and diffuse irradiances. Two versions of the RSS were designed at the Atmospheric Sciences Research Center at the State University of New York at Albany to measure UV from 295-370 nm and VIS-NIR from 360-1050 nm. A number of prototypes have been deployed at two sites of DOE's Atmospheric Radiation Measurement program since 1996. The first commercial UV RSS built by Yankee Environmental Systems, Inc. was deployed in 2001 and the VIS-NIR RSS is slated for permanent installation at the ARM SGP site in 2002. The paper describes instrument characterization procedures, spectral and radiometric calibrations. Mathematical algorithms applied to the spectra to correct wavelength shifts, to reduce stray light effects, and to correct drifts in radiometric calibration are described.

Keywords: UV-NIR, radiometry, shadowband, spectrograph, calibration, stray light, non-linearity, CCD.

1. INTRODUCTION

The Atmospheric Sciences Research Center (ASRC) extended the spectral coverage of the Multifilter Rotating Shadowband Radiometers (MFRSR)[1] using a two-prism detector array based spectrograph design. This design was selected to satisfy the high signal-to-noise ratio requirement of the shadowband measurement. The development of Rotating Shadowband Spectroradiometers (RSS) began at the ASRC seven years ago. To meet the demand of high dynamic range in the UVA and UVB regions one instrument (UV RSS) was optimized to cover 290-380 nm and the other (VIS-NIR RSS) was optimized to cover 360-1100 nm. The development of an instrument for the remaining NIR segment of the shortwave region was less pressing as the benefits of the shadowbanding technique are less apparent due to the fact that the diffuse irradiance in 1100-3000 nm amounts to only about $5Wm^{-2}$ for a clear sky. The UV and VIS-NIR RSS's share the same opto-mechanical design[2]. However, to improve out-of-band rejection, the UV-RSS has higher quality optics and is equipped with an additional fore-optic module.

Initially, a 512-pixel NMOS diode array (Hamamatsu Photonics K. K.) was used. Several versions of the VIS-NIR RSS with this detector participated in field campaigns within the Atmospheric Radiation Measurement (ARM) program in the course of the last five years. These field campaigns resulted in quality direct, diffuse, and total irradiance data that found applications in precise aerosol optical depth retrievals[3], water vapor retrievals[4,5], extraterrestrial irradiance estimates[6], photon path determination[7,8], verification of radiative transfer models[9] and retrievals from diffuse irradiance[10]. The UV RSS was first tested during the 1997 North American Ultraviolet Intercomparison[11], but the NMOS array did not provide sufficient sensitivity to do the shadowbanding; only total horizontal irradiance was measured. In the summer of 1998 we began using the 256x1024 open electrode CCD (Marconi-EEV) in VIS-NIR RSS's. This higher sensitivity and resolution VIS-NIR instrument operated at the Southern Great Plains (SGP) ARM site from July 1999 to September 2000, and its data were used to determine the extraterrestrial irradiance[6]. The higher sensitivity UV instrument was tested at the ASRC in Albany, New York, in July 2001 where the feasibility of shadowbanding was proven, permitting ozone retrievals from direct irradiance[12]. The same UV instrument participated in a diffuse irradiance experiment at the SGP ARM site in October 2001. In parallel with the work at ASRC on the research instruments, Yankee Environmental Systems, Inc. worked toward viable commercial instruments that are based on similar designs. The commercial UV instrument was deployed at Table Mt. in Boulder, Colorado, in June 2001 and the commercial VIS-NIR instrument is slated for permanent installation at the SGP in 2002. In this paper we give a detailed description of the characterization of the VIS-NIR RSS and then we focus on data processing that is employed to reduce errors from identifiable sources. All calculations and examples use data from the VIS-NIR RSS when it was deployed at SGP in 1999-2000 except when UV-RSS data from July 2001 are used to illustrate the non-linearity characterization and correction.

*kiedron@asrc.cestm.albany.edu; phone (518)437-8737; fax (518)437-8711; Atmospheric Sciences Research Center, State University of New York at Albany, 251 Fuller Road, Albany, NY, USA 12203

2. INSTRUMENT DESCRIPTION

The optics of the VIS-NIR RSS is depicted in Figure 1 with the actual ray-trace. The design and optical elements were selected to maximize throughput and minimize the stray light. For this reason refractive rather than reflective optics were chosen. All lenses are plano-convex singlets; achromatization was not attempted to keep the number of surfaces to a minimum. Because of the chromatic aberrations, the image plane is oblique to the optical axis. For this reason the CCD reflects some of impinging light away from the optical system into the dark cavity. The CCD has no window to avoid reflections between the window and the surface of the CCD.
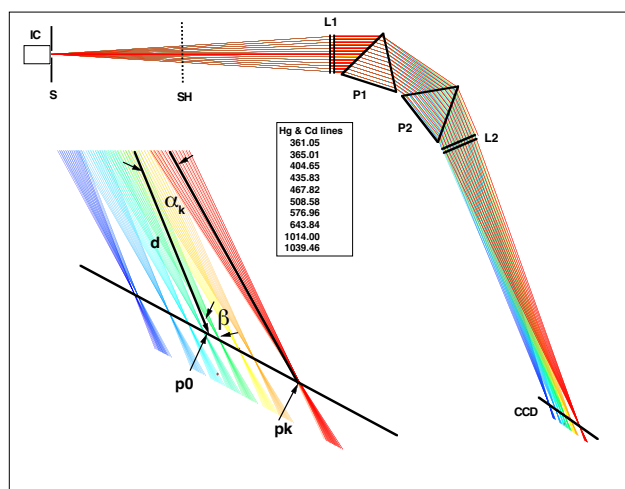

Figure 1: VIS-NIR RSS optics (IC-integrating cavity, S-slit, SH-shutter, L1-collimating lens, P1,P2-prisms, L2-camera lens, CCD-charge couple device array).

The slit image is formed on the two dimensional CCD (Figure 2) but during the operation all rows within the image are binned during a single readout. The binning reduces the effect of the read noise but diminishes the dynamic range. The exposure is selected prior to the shadowbanding to utilize the dynamic range of the CCD. Exposures can vary between 0.25-5 seconds, which in combination with 16-bit readout row capacity results in 20+ bits combined dynamic range if noise is included. The CCD is electronically shuttered, which means that the shutter is open when image rows are binned into the readout row. This introduces slight exposure non-linearity for short exposures, but assures more precise and reproducible
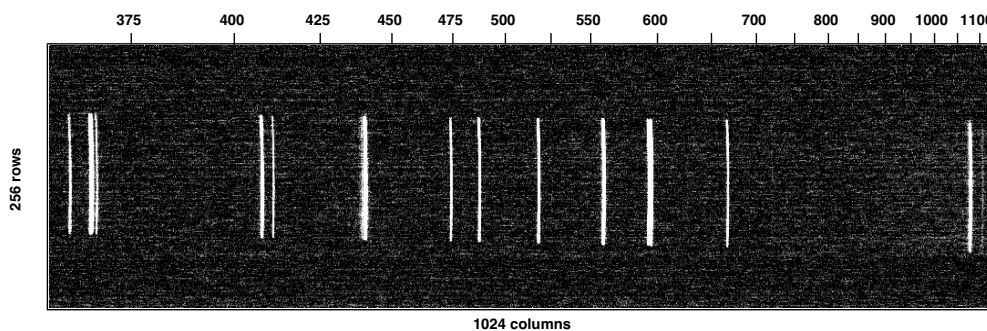

Figure 2: Image of Hg and Cd lines recorded by the CCD.

exposure times than with a mechanical shutter. At the end of each shadowbanding cycle the mechanical shutter is closed to acquire dark signal at the same exposure time that was used to measure signals in four positions of the shadowband. To keep dark counts low and constant the CCD is held at 5°C with a PID-controlled thermoelectric cooler. Currently RSS instruments use a 256x1024 CCD-30-11 (Marconi-EEV) that is of the open electrode type. It has 26μmx26μm pixels. Its cost is significantly lower than back-thinned CCD's with a comparable quantum efficiency and without etaloning problems.

3. INSTRUMENT CHARACTERIZATION

3.1 Non-linearity

Non-linearity originates in the CCD plus electronics and from exposure time for short exposures. These two non-linear effects can be factorized. Thus the linearized $\hat{C}$ counts per second is a function of measured counts C and exposure E:

$$\hat{C} = \frac{f(C)}{E \cdot d(E)} \tag{1}$$

For small values of C, $f(C)$ is practically linear. Therefore the function $d(E)$ can be determined by measuring a stable low intensity source at multiple exposures. In Figure 3 $d(E)$ is depicted. We do not know of any effect that could change $d(E)$ with aging of the instrument.
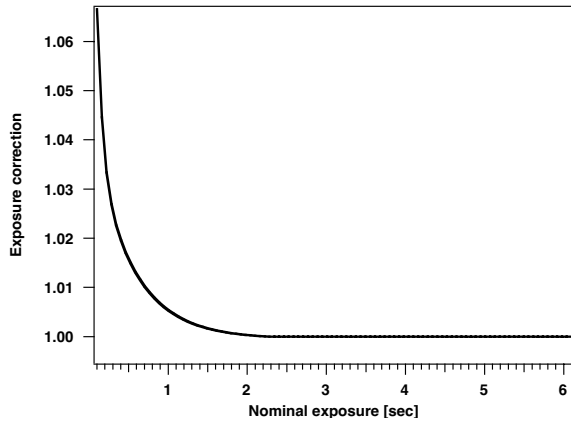

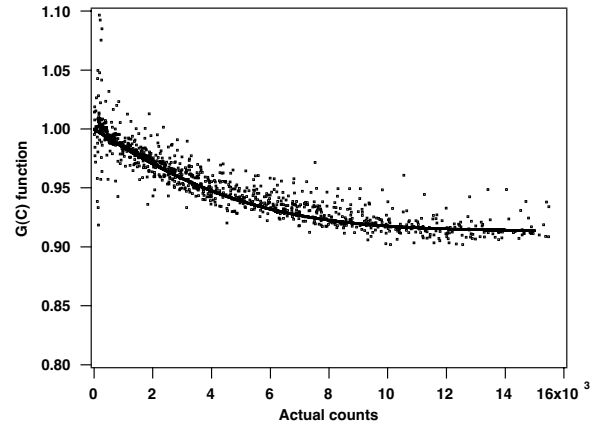Figure 3: Exposure correction function $d(E)$.

Figure 4: Function $g(C)$ fitted to experimental values for UV RSS(2001).

Let's denote by $C(p,I)$ measured counts at pixel p for exposure E and for irradiance I. Then the following expression:

$$g(C) = C(p, I_k) \approx \frac{I_k - I_{k+1}}{I_k} \frac{C(p, I_k)}{C(p, I_k) - C(p, I_{k+1})} \tag{2}$$

can be calculated from measurement data (see Figure 4). A surrogate irradiance instead of actual irradiance can be used. When inverse square law measurements are possible, i.e., when a strong "point" source is available, $I \propto 1/r^2$. When it is not the case, as in UV, exposure can be used as a surrogate irradiance, but then $C(p, I_k)/d(E)$ instead of $C(p, I_k)$ needs to be used in (2). The difference equation (2) leads to the following differential equation:

$$g(C) = \frac{C}{f(C)} \frac{df(C)}{dC} \tag{3}$$

that has the following solution:

$$f(C) = ACe^{\int \frac{g(c)-1}{c} dc} \qquad (4)$$

The function $g(C)$ is a measure of non-linearity. In the presented case of the UV RSS in 2001 the CCD electronics was not optimally tuned and the nonlinearity approached 10% (Figure 4), but after the characterization, by using (1), the non-linearity was reduced to less than 0.5%. In the case of the VIS-NIR instrument (1999-2000) the non-linearity was less that 1% without a correction. It is worth noting that for more precise non-linearity characterization the source superposition method is preferable[13]. Then the solution of a functional equation is sought; it can be estimated with a polynomial by the least square regression[14].

3.2 Shadowbanding cycle
During one shadowbanding cycle five measurements, including dark signal, are performed. In Figure 5 three shadowband positions (two corrections and blocked) with respect to the diffuser are presented. The counts of direct and diffuse horizontal irradiances can be obtained from the following equations:

$$C_{Diff} = C_{Tot} - \tfrac{1}{2}(C_- + C_+) + C_{Blocked} - C_{Dark} \qquad (5)$$

$$C_{Dir} = \tfrac{1}{2}(C_- + C_+) - C_{Blocked} \qquad (6)$$

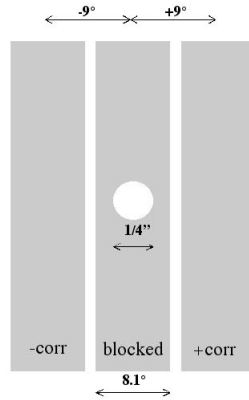$$C_{DirNorm} = C_{Dir}/\cos(SZA) \qquad (7)$$

Figure 5: RSS shadowbanding geometry.

Equations 5-7 overestimate direct and underestimate diffuse because the correction $\tfrac{1}{2}(C_- + C_+)$ does not eliminate all errors resulting from the 8.1° FOV angle. The estimates will have larger bias for an aerosol size distribution $n(r) = Ar^{-v}$ when v is small. The estimation of these errors for the shadowbanding geometry of the RSS were not completed, however, for typical $v = 4.2\text{-}4.4$ and a circular aperture of 8° the optical depth retrieved would be underestimated by 2%-5% without any correction[15], so we may expect that the RSS partial correction scheme presented above, should produce smaller errors than this.

3.3 Angular response
The integrating cavity is made of Spectralon. Similar integrating cavities were used in MFRSR's[1]. The angular response is measured at all pixels in ±89° zenith-angle range in two perpendicular azimuthal planes using a collimated Xe arc lamp[16] beam. In Figure 6 an example of angular response surface normalized by cosine of zenith angle is depicted. The angular response is wavelength dependent. For each wavelength and for SZA and SAA the direct normal irradiance must be corrected. The correction factor also must be applied to diffuse irradiance. It is calculated from the formula:

$$D_{corr} = \frac{\iint \sin(2\zeta)A(\alpha,\zeta)R(\alpha,\zeta)d\alpha d\zeta}{\iint \sin(2\zeta)R(\alpha,\zeta)d\alpha d\zeta}$$

(8)

.

where $A(\alpha,\zeta)$ and $R(\alpha,\zeta)$ are angular response and sky radiance, respectively, as functions of azimuth and zenith angles. In Figure 7 D_{corr} for several sky radiance models is calculated. At large angles of incidence the integrating cavity, chiefly because of the first air-Spectralon interface, exhibits polarization sensitivity. The polarization sensitivity may introduce error in the diffuse irradiance measurement for cloudless, low turbidity skies. As the sun moves from zenith to horizon this error changes from -1.5% and +1% [17].
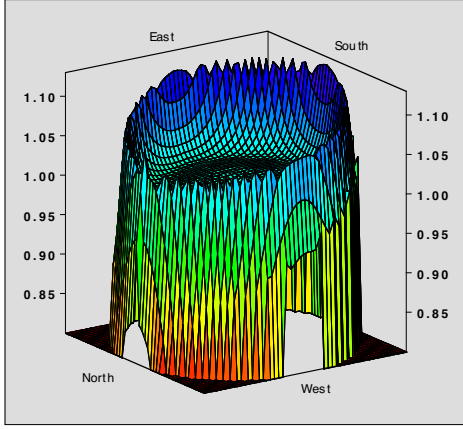

Figure 6: Normalized angular response for non-polarized light.
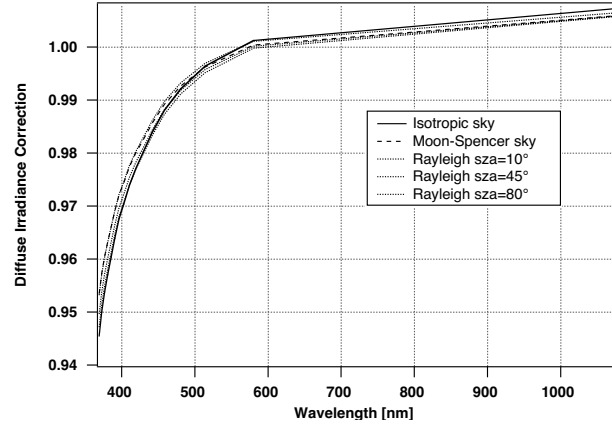

Figure 7: Diffuse irradiance correction.

3.4 Wavelength calibration and resolution

Wavelength to pixel mapping is nonlinear. In the first approximation the linearization can be obtained via the index of refraction $n(\lambda)$ of fused silica[18]. The centroids of spectral lines can be fitted to the second order polynomial of index of refraction (9). The polynomial fit does not have physical constraints, so in cases when few spectral lines were measured or

$$\min_{a,b,c} \sum_k (p_k - c - b \cdot n(\lambda_k) - a \cdot n(\lambda_k)^2)^2$$

(9)

when some centroids are biased with large errors, the wavelength calibration might be inaccurate. We devised a method that has physical constraints based on the design of the RSS spectrograph. A paraxial ray trace (see Figure 8 and equations 10)
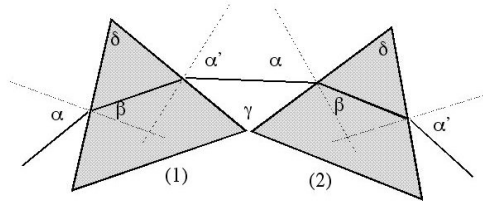

Figure 8: Illustration for paraxial ray trace calculations

$$\beta_1 = \sin^{-1}\left(\tfrac{1}{n}\sin(\alpha_1)\right)$$

$$\alpha_1' = \sin^{-1}(n\sin(\delta_1 - \beta_1))$$

$$\beta_2 = \sin^{-1}\left(\tfrac{1}{n}\sin(\gamma - \alpha_1')\right) \tag{10}$$

$$\alpha_2' = \sin^{-1}(n\sin(\delta_2 - \beta_2))$$

$$\alpha(\lambda_k) = \alpha_2'(\lambda_k) - \alpha_2'(\lambda_{min})$$

is performed to obtain angles of deviation $\alpha(\lambda_k)$ for wavelengths λ_k of measured spectral lines for design parameters of the optical system. The centroids' positions can be calculated from (11) where p_0 is a pixel for minimum deviation condition, d is distance from p_0 to lens L2 and β is image plane tilt angle (see Figure 1). Additionally, prism temperature is also a free

$$\hat{p}_k = p_0 + d\,\frac{\sin(\alpha(\lambda_k))}{\sin(\alpha(\lambda_k) + \beta)} \tag{11}$$

$$\min_{p_0,d,\beta,T}\ \sum_k (p_k - \hat{p}_k)^2 \tag{12}$$

parameter. All four parameters are used to minimize the difference between measured and calculated centroids. Results of this optimization are presented in Figure 9.
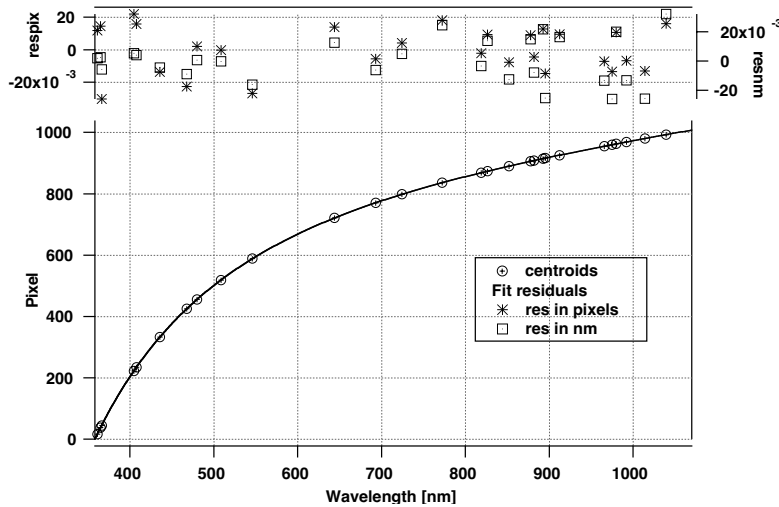

Figure 9: Wavelength calibration curve obtained from fit to
lines of Cd, Hg, Ar, Kr, Ne and Xe, and residuals.

The centroids are obtained by fitting a sum truncated Gaussian function 1st degree polynomial to remove the baseline. The FWHM of each line is also estimated. In Figure 10 FWHM expressed in pixels is estimated as a function of pixels. The dependence of resolution on pixels results from the fact that image is not exactly flat, so not all wavelengths have their focus on the CCD. In Figure 11 the FWHM is expressed in nanometers. Wavelength stability depends on mechanical factors and on the index of refraction. The index of refraction of fused silica has relatively large temperature coefficient and the index of refraction of air that surrounds the prisms depends on pressure. In Figures 12 and 13 we show wavelength and pixel shifts as functions of wavelength and temperature and pressure change. Wavelength sensitivity to optical element dislocations (translations and rotations) was analyzed using three dimensional ray tracing. The results are summarized in Table 1. All perturbations in the second column produce a maximum 0.25 pixel spectrum shift in some parts of a spectrum. The shifts are pixel dependent, but the dominant relationship is linear $\Delta p = Ap + B$ and the second order correction (see column 5) is very small. The optical system has no moving parts, so perturbation of individual optical elements is not likely. The expansion of the aluminum plate ($\Delta t = 10°C$) causes only a 0.17 pixel shift (see the last row). It must be noted that the temperature of the optics and optical box are held to better than 0.2°C.
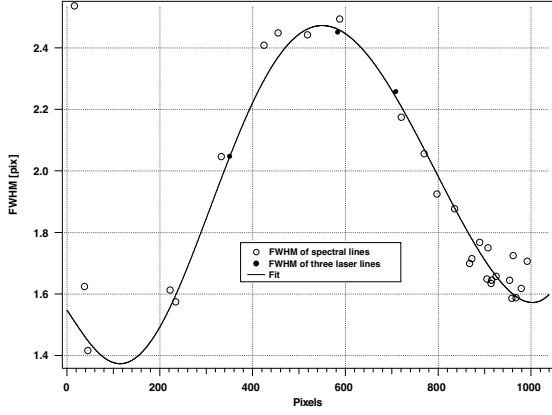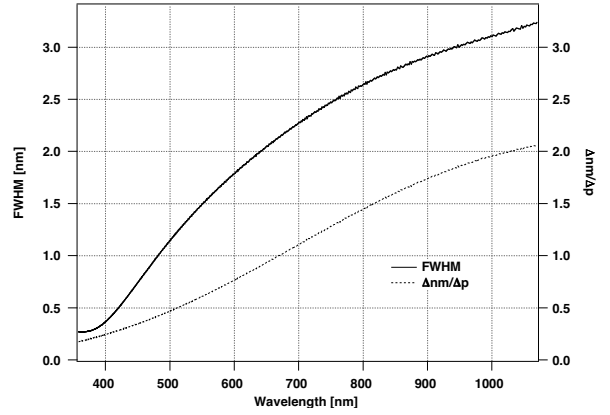
Figure 10: FWHM in pixels.

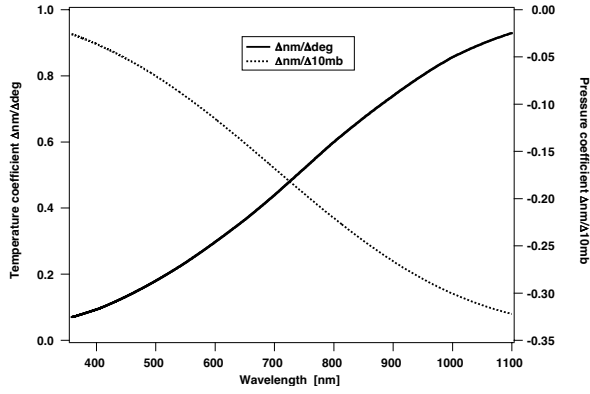Figure 11: FWHM in nanometers and Δnm/p.

Figure 13: Fused silica temperature and air pressure wavelength effects expressed in nanometers.
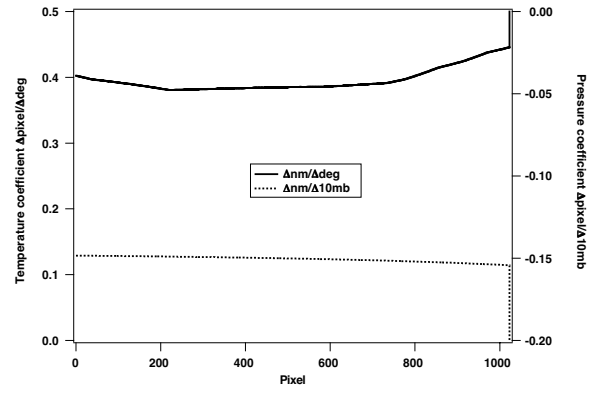

Figure 14: Fused silica temperature and air pressure wavelength effects expressed in pixels.

Table 1: Pixel shifts $\Delta p = Ap + B$ due to optical elements translations and rotation.

Optical Element	Perturbation	B [pixels]	A	Curvature [pixels]
Slit	Δx=0.0035mm	-0.2260	-0.00001510	0.0050
Lens1	Δx=0.3800mm	-0.1191	0.00036960	0.0024
Lens1	Δy=0.0037mm	0.2480	0.00000628	0.0025
Lens1	Δß=0.1200°	0.2506	0.00000897	0.0003
Prism1	Δx=0.2100mm	0.2556	-0.00042418	0.0250
Prism1	Δy=0.7100mm	-0.2551	0.00041304	0.0126
Prism1	Δß=0.0770°	-0.2550	0.00045212	0.0204
Prism2	Δx=0.3000mm	0.2510	-0.00040398	0.0080
Prism2	Δy=0.2550mm	-0.2498	0.00039630	0.0026
Prism2	Δß=0.0250°	-0.2528	0.00048254	0.0019
Lens2	Δx=0.0039mm	0.2270	0.00003152	0.0007
Lens2	Δy=0.0085mm	0.1800	0.00007159	0.0015
Lens2	Δß=0.1850°	0.2367	0.00001415	0.0054
CCD	Δß=0.0180°	0.2546	-0.00045580	0.0173
Thermal Expansion	Δt=10.000°C	-0.1514	0.00028465	0.0014

3.5 Radiometric calibration

Radiometric calibration is performed using NIST traceable incandescent lamps.   The responsivity is obtained as a ratio of measured counts to the irradiance of the source used for calibration (see Figure 15). The precision of calibration is dominated by the precision of reported irradiance[19,20].

3.6 Noise estimation

The noise of the CCD consists of read noise and Poisson photon noise:

$$\sigma = \sqrt{2\sigma_{read}^2 + (C + C_{Dark})/\eta} \tag{13}$$

where η is the coefficient that converts counts to photo-electrons. Both the standard deviation of the read noise and η can be determined by fitting (13) to measured the standard deviations of net counts $C - C_{Dark}$ for all pixels for various exposures and irradiances (see Figure 16).
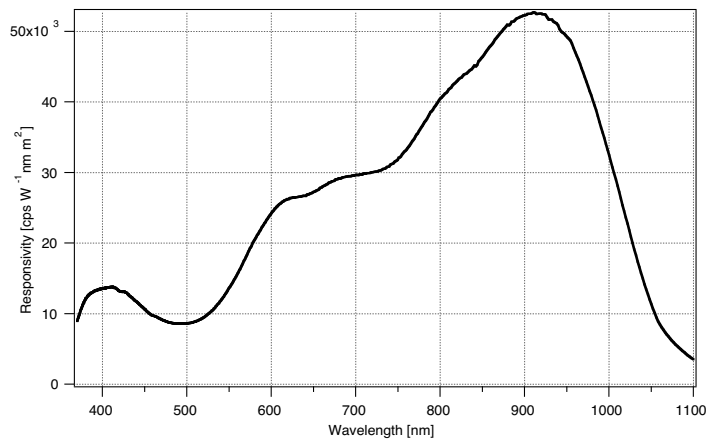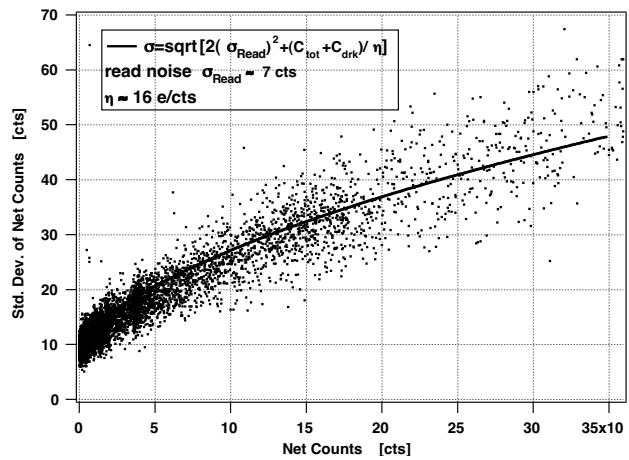
Figure 15: Responsivity of VIS-NIR RSS.

Figure 16: Standard deviation of noise: read noise ≈ 6.5cts.

From (5) and (6) we can estimate standard deviation of noise for each pixel in diffuse irradiance and direct irradiance in real time from the following formulas:

$$\sigma_{Diff} = \sqrt{\tfrac{7}{2}\sigma^2_{read} + (C_{Tot} + \tfrac{1}{2}(C_- + C_+) + C_{Blocked} + C_{Dark})/\eta} \qquad (14)$$

$$\sigma_{Dir} = \sqrt{\tfrac{3}{2}\sigma^2_{read} + (\tfrac{1}{2}(C_- + C_+) + C_{Blocked})/\eta} \qquad (15)$$

3.7 Out-of-band rejection
Out-of-band rejection is defined by the stray light in the optical system. It must be measured with strong quasi-monochromatic sources using short and long exposures or attenuators to obtain separately the wings and the central part of the slit-scattering function. The wings and the central part are spliced. The scattering originates on six surfaces of optical elements and in the bulk of fused silica.   The optical elements for VIS-NIR instrument are of 60-40 scratch-and-dig quality while for the UV instrument lenses and prisms are 10-5 and 20-10 scratch-and-dig, respectively. The effects from multiple reflections within and between lenses are negligible. However, within each prism three reflections (a recycled beam effect) cause artifacts that are less than 10^{-4} for non-coated prisms. For wavelengths close to the minimal deviation path the recycled beams focuses are close to the image plane resulting in sharper artifacts (see Figure 17). The recycled beam effect can be reduced significantly with anti-reflective coatings or could be eliminated if the base surface of each prism was tilted with respect to the meridional plane by a few degrees. Then the recycled beam would travel above or below the image.
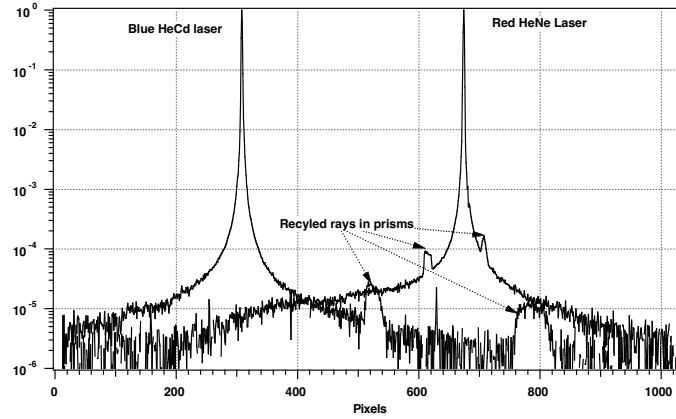

Figure 17: Slit scattering function.

3.8 Instrument mathematical model
Characterization of the instrument allows a formulation of a mathematical model that links irradiance to the measured counts as an integral operator:

$$C(p) = \int I(p')r(p')s(p,p')dp' \qquad (16)$$

$$I_{RSS}(p) = C(p)/R(p) \qquad (17)$$

where $s(p,p')$ is the slit spread function and $r(p)$ is quasi-monochromatic responsivity, $I(p)$ is quasi-monochromatic irradiance and $R(p)$ is responsivity as defined in the section 3.5. The quasi-monochromatic responsivity can be obtained by solving the integral equation (16) when $C(p)$ and $I(p)$ and $s(p,p')$ are known. Most difficult is the construction of the slit-spread function. The slit scattering functions and FWHM are interpolated and the array 1024x2048 of $s(p,p')$ values is generated. The mathematical model of the instrument is used when comparing results from radiatiave transfer modeling[9] with RSS measured spectra or when comparing RSS with other measurements, particularly from instruments of higher spectral resolution.

4. FORMULAS AND ALGORITHMS

4.1 Wavelength shift correction

Determination of wavelength correction is relatively easy because the RSS can resolve many Fraunhofer lines. Only for large solar-zenith angles when the signal is low is there an insufficient signal-to-noise ratio. The primary wavelength calibration is based on the lines of the spectral lamps. When it is performed in the field, a solar spectrum is measured when lamps are changed. These solar spectra, or actually, total horizontal counts can be used as a reference spectrum with which subsequent spectra are compared and wavelength changes are determined. One method of wavelength change determination is based on measuring centroids of selected Fraunhofer lines. Unlike scanning spectrometers, RSS wavelength changes are well behaved because all spectral elements of the spectrum are acquired at the same time. This means that we may expect only wavelength changes from one shadowbanding cycle to another following the linear function $\Delta p = Ap + B$. Coefficients A and B can be determined by shifting and stretching the reference spectrum to minimize some function of merit that compares the reference and measured spectra. The total horizontal counts can be conditioned to remove a low frequency envelope that depends on atmospheric conditions and responsivity of the instrument that might be drifting. The following filter applied to counts produces such a signal:

$$\overline{C}(p) = \frac{d}{dp}\left\langle \frac{C(p) - \langle C(p)\rangle_5}{\left\langle \left| C(p) - \langle C(p)\rangle_5 \right| \right\rangle_{31}} \right\rangle_5 \tag{17}$$

where $\langle\cdot\rangle_k$ denotes a moving average of k-length. The effect of the denominator in (17) makes the amplitudes comparable between different spectra (see Figure 18).
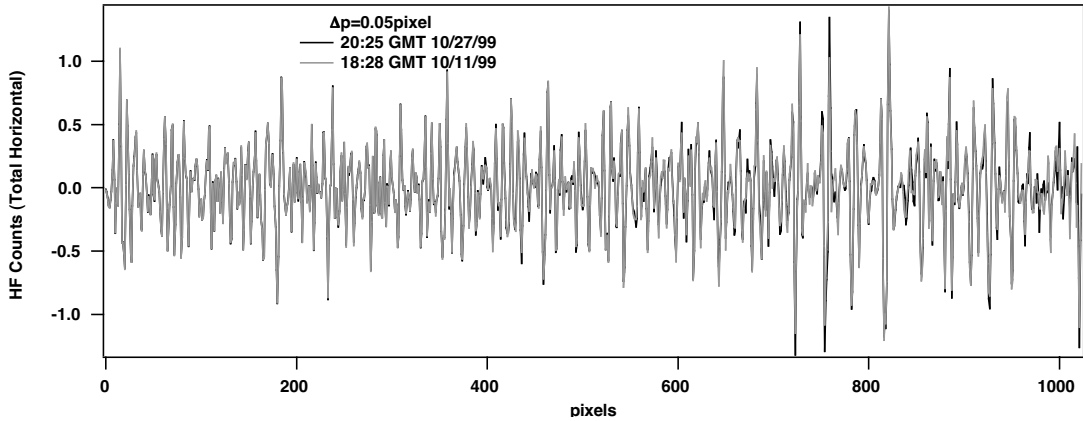

Figure 18: Two filtered spectra

When $|1024A|<<B$, which is the case when temperature or pressure effects are dominant, B is determined directly using Fourier transform shift-property from the following formula:

$$\Delta p = B = \frac{1}{2\pi}\arg\left(\frac{F\{\overline{C}(p)\}}{F\{\overline{C}_{ref}(p)\}}\right) \tag{18}$$
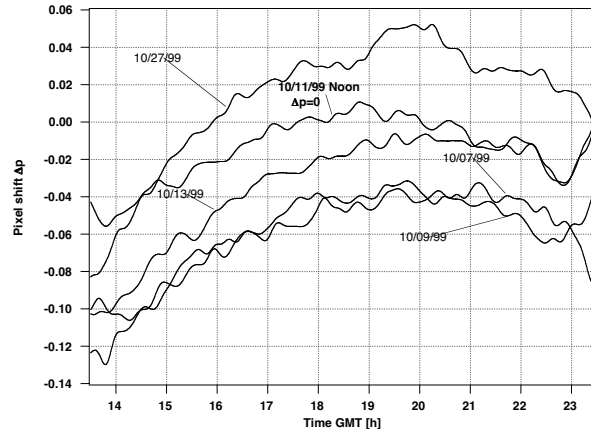
Figure 19: Pixel shift with respect to solar noon spectrum on 10/11/99 for five days as function of time.

A more robust result is obtained finding the centroid of the peak of the following function:

$$\left| F^{-1}\left\{ \frac{F\{\overline{C}(p)\}}{F\{\overline{C}_{ref}(p)\}} \right\} \right| \tag{19}$$

The method (19) was used to determine the wavelength of each spectrum measured during five days with respect to one reference spectrum (see Figure 19). Note that shifts vary between -0.12 pixel and +0.05 pixel. This could be attributed to temperature changes of less then ±0.125°C or pressure changes of less than ±5 mb. There is evidence for some correlation of the shifts with the ambient temperature that varied between 20-35°C, however, we could not verify pressure changes, as the pressure sensor was inactive during this deployment of the RSS.

4.2 Stray light reduction

Various deconvolution methods can be used to reduce the stray light and improve out-of-band rejection[22]. The deconvolution methods were designed for the super-resolution problem that is inherently ill-posed. The reduction of stray light is not concerned with restoring of missing high frequencies, but with removing some low frequency components, and it results in removing energy carried by the wings of the slit spread function back to the centers. The method described here is approximate and is akin to the first step in the iterative process of the Jacobi method[23]. The integral operator (16) is rewritten as follows:

$$C(p) = \int c(p')s(p,p')\,dp' \tag{20}$$

where $c(p)$ denotes quasi-monochromatic counts. The slit-spread function is a sum of two components

$$s(p,p') = s_c(p,p') + s_w(p,p') \tag{21}$$

that are defined as follows:

$$s_c(p,p') = s(p,p') \quad \left| p - p' \right| \leq \tfrac{1}{2}\Delta_p$$
$$s_w(p,p') = s(p,p') \quad \left| p - p' \right| > \tfrac{1}{2}\Delta_p \tag{22}$$

These components can be normalized with pixel dependent coefficients

$$a = \int s(p,p')\,dp' \quad a_c = \int s_c(p,p')\,dp' \quad a_w = \int s_w(p,p')\,dp' \tag{23}$$

Now we may define counts that have no stray light outside the intervals $\Delta_p < p < \Delta_p$:

$$\hat{C}(p) = \frac{a}{a_c} \int c(p') s_c(p, p') dp' \qquad (24)$$

The coefficient in the front of the integral in (24) preserves the energy of the signal. Then

$$\hat{C}(p) = \frac{a}{a_c} \left[C(p) - \int c(p') s_w(p, p') dp' \right] \qquad (25)$$

We do not know $c(p)$ in (25), so we replace it with measured counts $C(p)$, leading to the following approximation:

$$\hat{C}(p) \approx \tilde{C}(p) = \frac{a}{a_c} \left[C(p) - \int C(p') s_w(p, p') dp' \right] \qquad (26)$$

First we use (20) and (24) to calculate $C(p)/\hat{C}(p)$ in order to estimate the effect in the stray light. The results are presented in Figures 20 and 21 for direct and diffuse synthetic spectra. The stray light effect, as expected, affects strong absorption bands, and it is larger in the diffuse irradiance. It can be shown that

$$\left| \tilde{C}(p) - \hat{C}(p) \right| < a_w \frac{a}{a_c} c_{max} \approx a_w c_{max} \qquad (27)$$

which shows that errors of the approximations (26) are small because a_w is small, however (27) overestimates these errors. The ratios $\tilde{C}(p)/\hat{C}(p)$ that were calculated for synthetic spectra (see Figure 22) demonstrate that the errors of approximation (26) are negligible and that they may increase for more aggressive stray light removal when Δ_p gets too small. The presented method increases the signal-to-nose ratio only by a factor of 1.04.
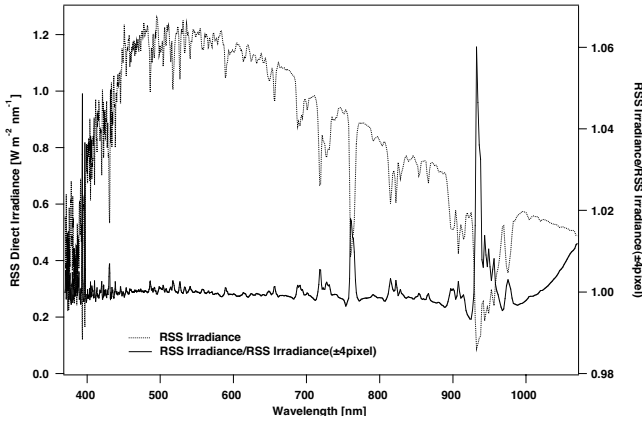
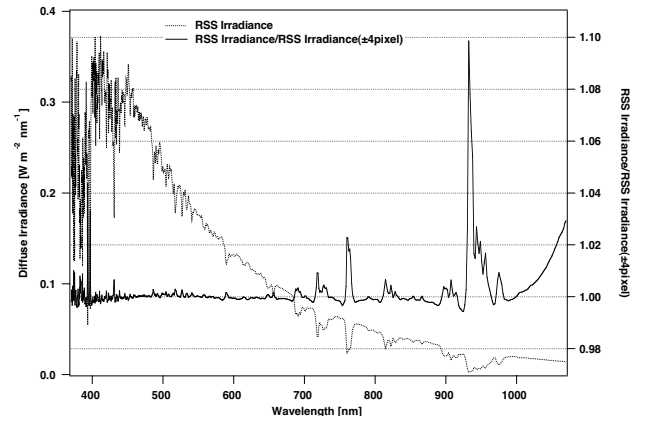

Figure 20: Direct irradiance and fraction of stray light.

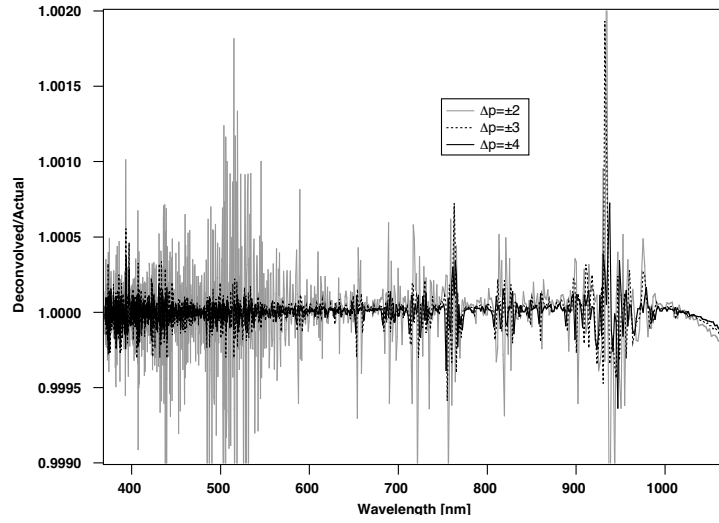Figure 21: Diffuse irradiance and fraction of stray light.

Figure 22: Simulated errors of the approximate stray light removal method

4.3 Correction for non-Lambertian angular response

The angular response is used to correct direct normal (7)

$$\hat{C}_{DirNorm} = C_{DirNorm} \, / \, A(SAA, SZA)$$

(28)

and the factor (8) is used to correct diffuse irradiance:

$$\hat{C}_{Diff} = C_{Diff} \, / \, D_{corr}$$

(29)

4.4 Responsivity drift correction

Instrument responsivity changes with time due to throughput degradation and CCD quantum efficiency changes. The drift can be monitored by performing Langley regression[24] on clear days.

$$\min_{C_0, \tau} \sum_{2 < m < 6} \left(\ln(C_{DirNorm}(m)) - \ln(C_0) - \tau \cdot m - \tau_X m_X \right)^2 \quad X = H_2O, O_x, NO_x$$

(30)

The coefficients C_0 can be found for all pixels if optical depth of major absorbers is removed. This can be done for O_2 as its column is known and the varying column of H_2O can be retrieved quite accurately without accurate knowledge of responsivity within the absorption bands of H_2O. Usually the effects of O_3 and NO_2 on the C_0 in Langley regression are negligible. C_0 from a single Langley event has large uncertainty. To estimate responsivity drift, C_0 from multiple Langley events are used.

$$\min_{a,b,c} \sum_{n - \Delta(n) < k < n + \Delta(n)} (C_0(t_k) - c_n - b_n \cdot t_k - a_n \cdot t_k^2)^2$$

(31)

A moving average[25] or a moving fit of 1st or 2nd degree polynomial, as in (31), can be used to calculate C_0 for any given day t_n from the formula:

$$\hat{C}_0(t_n) = c_n + b_n \cdot t_n + a_n \cdot t_n^2$$

(32)

Then one can estimate responsivity from day t_m to day t_n

$$R(t_n) = \frac{\hat{C}_0(t_n)}{\hat{C}_0(t_m)} R(t_m) \qquad (33)$$

Also the extraterrestrial irradiance could be used to obtain the responsivity

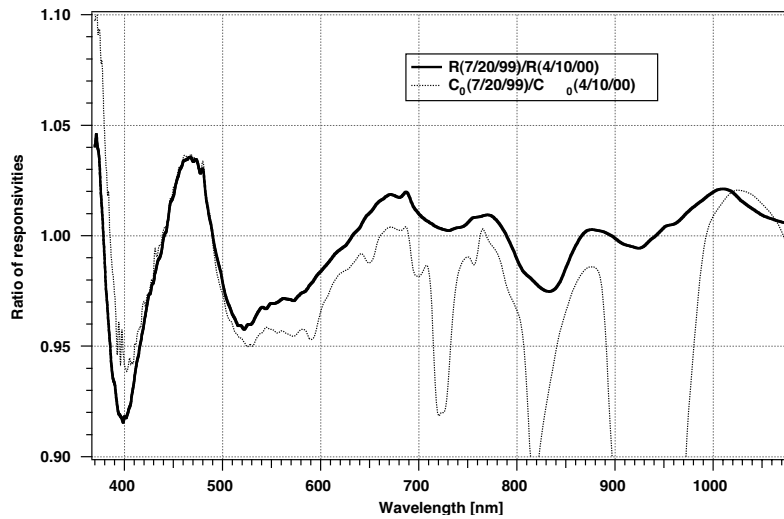$$R(t_n) = \hat{C}_0(t_n) / I_{ET} \qquad (34)$$

Figure 23: Ratio of responsivities from lamp calibrations and ratio of C_0 predicted from the set of Langley events

The method described by (31), (32) and (33) was used to track responsivity drift during the deployment between June 1999 and September 2000. Three lamp calibrations were performed. They indicated large changes in resposnivity in 380-500nm range. The same changes were predicted from the Langley process and responsivities for days between lamp calibrations could be determined (see Figure 23).

5. SUMMARY

In this paper we described the process of RSS characterization and methods used to improve quality of the data by correcting and reducing various errors. We recapitulate the order in which corrections need to be performed: (1) non-linearity correction, (2) wavelength correction, (3) stray light correction, (4) responsivity correction, (5) angular response correction.

ACKNOWLEDGEMENTS

REFERENCES

1. L.Harrison, J.Michalsky and J.Berndt, "Automated multifilter rotating shadow-bandradiometer: An instrument for optical depth and radiation measurements", *Appl.Opt*. **33**, pp.5118-5125, 1994.
2. L. Harrison, M. Beauharnois, J. Berndt, P. Kiedron, J. Michalsky and Q. Min, "The rotating shadowband spectroradiometer (RSS) at SGP", *Geophys. Res. Lett*., **26**, pp.1,715-1,718, 1999.

3. J. Michalsky, M. Beauharnois, J. Berndt, L. Harrison, P .Kiedron and Q. Min, "O2-O2 absorption band identification based on optical depth spectra of the visible and near-infrared," *Geophys. Res. Lett.* **26**, pp.1581-1584, 1999.

4. J. J. Michalsky, Q. Min, P. W. Kiedron, D. W. Slater and J. C. Barnard, "A differential technique to retrieve column water vapor using sun radiometry," *J. Geophys .Res.* **106**, pp.17,433-17,442 2001.

5. P. Kiedron, J. Michalsky, B. Schmid, D. Slater, J. Berndt, L. Harrison, P. Racette, E. Westwater and Y. Han," A robust retrieval of water vapor column in dry Arctic conditions using the rotating shadowband spectroradiometer," *J. Geophys. Res.* **106**, pp.24,007-24,016 2001.

6. L. Harrison, P. Kiedron, J. Berndt and J. Schlemmer, "The extraterrestrial solar spectrum 360 to 1050 nm from rotating shadowband spectroradiometer (RSS) measurements at the Southern Great Plains (ARM) Site", *J. Geophys. Res.* (in print)

7. Q.-L. Min and L. Harrison, "Joint statistics of photon pathlength and cloud optical depth," *Geophys. Res. Lett.* **26**, pp.1425-1428, 1999.

8. Q. Min, L. C. Harrison and E. E. Clothiaux, "Joint statistics of photon pathlength andcloud optical depth: cases tudies," *J. Geophys .Res.* (in print)

9. E. J. Mlawer, S. A. Clough, P. D. Brown, L. Harrison, J. Michalsky, P. Kiedron, and T. R. Shippert, "Comparison of spectral direct and diffuse solar irradiance measurements and calculations for cloud-free conditions," *Geophys. Res. Lett.*, **27**, pp.2653-2656, 2000.

10. P. Kiedron, J. Berndt, L. Harrison, J. Michalsky and Q. Min **,"**Column water vapor from diffuse irradiance**,"** *Geophys. Res. Lett.* (submitted 2002)

11. K. Lantz, P. Disterhoft, J. DeLuisi, E. Early, A. Thompson, J. Berndt, L. Harrison, P. Kiedron, J. Ehramjian, G. Bernhard, L. Cabasug, J. Robertson, W. Mou, T. Taylor, J. Slusser, D. Bigelow, B. Durham, G. Janson, D. Hayes, M. Beaubien and A. Beaubien, "The 1997 North American Interagency Intercomparison of Ultraviolet Spectroradiometers including Narrowband Filter Radiometers," *J. Res. Natl. Inst. Stand. Tech.* (inprint)

12. P. W. Kiedron, L. H. Harrison, J. L. Berndt, J. J. Michalsky and A. F. Beaubien, "Specifications and performance of UV rotating shadowband spectroradiometer (UV-RSS)," *Proc. SPIE* **4482**, 2001.

13. C. L. Sanders, "A photocell linearity tester," *Appl. Optics*, **1**, pp.207-211, 1962.

14. L. Coslovi and F.Righini, "Fast determination of the nonlinearity of photodetectors," *Appl. Optics*, **19**, pp.3200-3203, 1980.

15. M. A. Box and A. Deepak, "Atmospheric scattering correction to solar radiometry," *Appl. Optics* **18**, pp.1941-1949, 1979.

16. J. J. Michalsky, L. H. Harrison, and W. E. Berheiser, "Cosine response characteristics of some radiometric and photometric sensors," *Solar Energy*, **54,** pp.397-402, 1995.

17. P. Kiedron and J.Michalsky, "Polarization sensitivity of diffusers used in MFRSR and RSS and diffuse irradiance errors," *Intl. J. Remote Sensing* (inprint).

18. I. H. Malitson, "Interspecimen comparison of the refractive index of fused silica," *J. Opt. Soc. Am.*, **55**, pp.1205-1209, 1965.

19. P. W. Kiedron, J. J. Michalsky, J. L. Berndt and L. C. Harrison, "Comparison of spectral irradiance standards used to calibrate shortwave radiometers and spectroradiometers," *Appl. Optics*, **38**, pp.2,432-2,439, 1999.

20. P. Kiedron, J. Berndt, J. Michalsky, D. Myers, A. Andreas, A. Bucholtz and F. P. J. Valero, "Absolute calibration of ARESEII spectrometers and spectral radiometers," *J. Geophys. Res.* (submitted).

21. H. Slaper, H. A. J. M. Reinen, M. Blumthaler, M. Huber and F.Kuik, "Comparing ground-level spectrally resolved solar UV measurements using various instruments: A technique resolving effects of wavelength shift and slit width," *Geophys. Res. Lett.*, **22**, pp.2721-2724, 1995.

22. P. A. Jansson. "Deconvolution : with applications in spectroscopy", New York, Academic Press, 1984.

23. T. Seim and S. Pydz, "Automated spectroradiometer applying computer analysis of spectral data," *Appl. Optics*, **11**, pp.1169-1177, 1972.

24. L. Harrison and J.Michalsky, "Objective algorithms for the retrieval of optical depths from ground-based measurements," *Appl.Opt.,* **33**, pp.5126-5132, 1994.

25. B. W. Forgan, "Sunphotometer calibration by the ratio-Langley method," Baseline Atmospheric Program (Australia 1996), eds. B. W. Forgan and P. J. Fraser, June 1998.